

High-Temperature Polarization-Free III-Nitride Solar Cells with Self-Cooling Effects

Xuanqi Huang,^{†,‡} Wei Li,^{§,‡} Houqiang Fu,[†] Dongying Li,[†] Chaomin Zhang,[†] Hong Chen,[†] Yi Fang,[†] Kai Fu,[†] Steven P. DenBaars,^{||} Shuji Nakamura,^{||} Stephen M. Goodnick,[†] Cun-Zheng Ning,[†] Shanhui Fan,^{*,§} and Yuji Zhao^{*,†}

[†]School of Electrical, Computer and Energy Engineering, Arizona State University, Tempe, Arizona 85287, United States

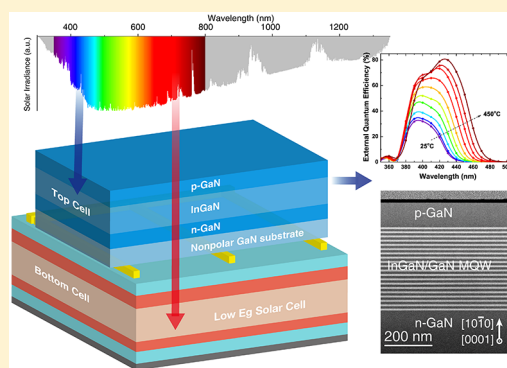
[§]Department of Electrical Engineering, Ginzton Laboratory, Stanford University, Stanford, California 94305, United States

^{||}Materials Department, University of California, Santa Barbara, California 93106, United States

Supporting Information

ABSTRACT: High-temperature photovoltaics (PV) for terrestrial and extraterrestrial applications have presented demanding challenges for current solar cell materials, such as Si, III–V AlGaInP, and II–VI. Wide-bandgap III-nitride materials, in contrast, offer several intrinsic advantages that make them extremely appealing for high-temperature applications. In this study, we fabricated and characterized III-nitride solar cells using polarization-free (i.e., nonpolar) InGaN/GaN multiple quantum wells (MQWs). The InGaN solar cells showed a large working temperature range from room temperature (RT) to 450 °C, with positive temperature coefficients up to 350 °C. The peak external quantum efficiencies of the devices showed a 2.5-fold enhancement from RT (~32%) to 450 °C (~81%), which is distinct from all other solar cells ever reported. This can be partially attributed to an increase of over 70% in carrier lifetime in nonpolar InGaN MQWs obtained from time-resolved photoluminescence. Furthermore, a thermal radiation analysis revealed a unique self-cooling effect for III-nitride materials, which also helps enhance device performance at high temperature. These results offer new insights and strategies for the design and fabrication of high-efficiency high-temperature PV cells.

KEYWORDS: III-nitrides, high temperature, solar cells, polarization-free, self-cooling



High-performance solar cells operating at high temperatures (e.g., >300 °C) are highly desired for high-temperature photovoltaic (PV) applications, such as space missions near the Sun,^{1–4} terrestrial photovoltaic thermal (PVT) hybrid solar collector systems,⁵ and concentrating solar power (CSP)/PV hybrid systems.⁶ For example, the perihelion distance of Mercury is 0.307 astronomical units (AU) from the Sun. This resulted in an extremely high temperature of ~400 °C at the Mercury planet surface,¹ presenting a significant challenge for the efficient generation of solar power for spacecraft in NASA missions. Similarly, high operation temperature (>300 °C) is also a critical requirement for the next-generation terrestrial PVT hybrid system due to the concentrated solar power.⁷ For CSP/PV hybrid systems, InGaN PV cells have been proposed to integrate with the current CSP systems as the photovoltaic topping cells.⁷ This simultaneously allows for the generation of electricity through sunlight and the storage of dispatchable heat that can theoretically improve the efficiency by 46% compared to the CSP system alone. The current high-temperature electronic technologies typically utilize an active cooling process, which is however undesirable in these applications, as it consumes a

large amount of power and reduces the total efficiency of the system. Therefore, there is an urgent need for developing solar cells based on new PV materials that enable efficient operation at high temperatures.

Solar cells based on conventional III–V semiconductors, e.g., GaAs,^{8,9} GaP/AlGaP,^{2,10} AlGaInP,¹¹ and even SiC,⁴ have been researched for high-temperature applications with limited success. The intrinsic PV conversion efficiency of these devices typically showed a sharp decrease with increasing temperatures; that is, these cells exhibit a negative temperature coefficient.^{9,12} For example, GaAs solar cells were reported with an absolute efficiency drop of 0.4% per 10-degree temperature increase at one-sun and failed shortly after exposure to high temperature.^{1,8} The escalating short-circuit current (J_{sc}) and dropping open-circuit voltage (V_{oc}) at high temperatures of these cells are also detrimental to the PV module operation. Furthermore, other extrinsic effects such as degradation in metal contacts further exacerbate the device performance at high temperature.^{13–15}

Received: May 1, 2019

Published: July 5, 2019

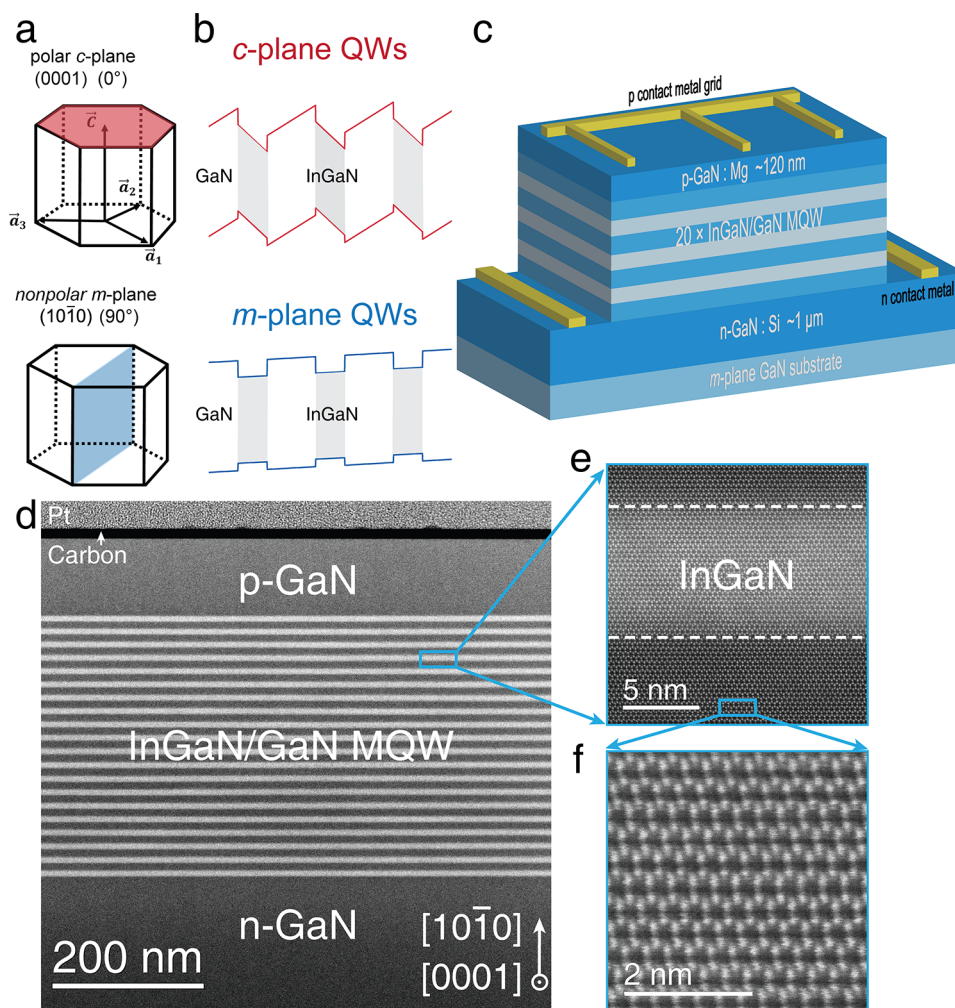


Figure 1. (a) Crystal planes of the polar *c*-plane (top) and the nonpolar *m*-plane GaN (bottom). (b) Schematic zoom-in energy band diagrams of the active InGaN/GaN MQW regions of the two crystal planes. (c) Schematic device structure for the fabricated nonpolar InGaN solar cell. (d–f) Cross-section HAADF-STEM images of the nonpolar *m*-plane InGaN/GaN MQW solar cell structure with 20 periods of InGaN(6 nm)/GaN(10 nm) MQWs. (d) HAADF-STEM image of the entire solar cell structure. (e) HAADF-STEM image of one InGaN/GaN QW on the atomic scale. The white dashed lines are estimated interfaces between InGaN QW and GaN barrier layers and also serve as a guide to eyes. (f) Zoom-in HAADF-STEM image of the GaN epilayer from (e). The hexagonal wurtzite structure of GaN can be clearly identified. Upward is the growth direction.

Wide-bandgap III-nitride InGaN materials have emerged as a promising candidate for high-temperature solar cells. $\text{In}_x\text{Ga}_{1-x}\text{N}$ alloys have a tunable direct bandgap from ultraviolet (GaN ~ 3.4 eV) to near-infrared (InN ~ 0.7 eV) spectral regions derived by changing the In compositions that provide a perfect match to the solar spectrum.^{16–19} Due to the relatively wider bandgap compared to Si or III–V, InGaN solar cells are also expected to have higher operation temperatures and superior radiation tolerance.^{15,17} These properties therefore make them particularly suitable for aforementioned space missions and terrestrial PVT hybrid systems. Despite these advantageous properties, InGaN solar cells are still a nascent field in PV due to well-known challenges in III-nitrides such as high defect density due to lack of native substrates.²⁰ The first demonstration of a III-nitride solar cell emerged around 2007 with an InGaN/GaN p–i–n double heterostructure (DH) grown on *c*-plane sapphire substrates.²¹ Later, it was realized that the performance of InGaN solar cells can be further improved by utilizing strained InGaN quantum wells (QWs) or superlattice active layer structures, similar to the commercial

III-nitride light-emitting diodes (LEDs).^{22–24} It was argued that these thin QW layers could mitigate defect formations that occur in thick InGaN layers and thus lead to improved device performance. With such an approach, single-junction InGaN QW solar cells with a relatively high external quantum efficiency of $\sim 50\%$ and decent J_{sc} and V_{oc} were demonstrated.^{23,25,26} Several groups also reported that the PV performance of InGaN QW solar cells can be reasonably sustained at high temperatures (e.g., 300 °C).^{27–30} Despite these encouraging progresses, these conventional InGaN solar cells unavoidably suffer from the polarization-related effects from the adoption of *c*-plane sapphire substrates, which have profound impacts on the efficiency of InGaN solar cells at both room temperature (RT) and high temperatures. At RT, the large polarization-induced electric field inside the InGaN/GaN QWs will lead to a large quantum barrier that hinders the carrier collection in solar cells.^{31,32} At high temperatures, the polarization-related effects are convoluted with thermal escaping, making it even more challenging to probe, analyze, and engineer the carrier dynamics of InGaN solar cells.

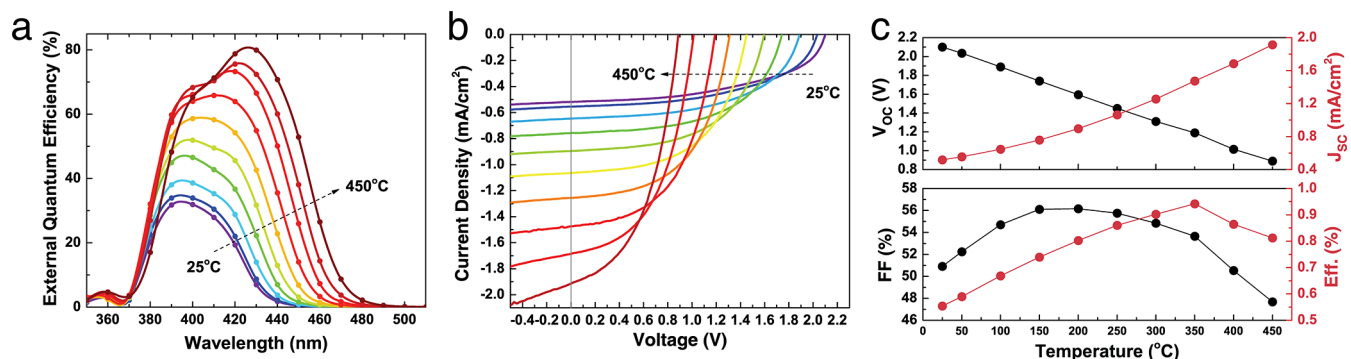


Figure 2. (a) Temperature-dependent EQE spectra of the nonpolar InGaN MQW solar cell at different temperatures from 25 to 450 °C. (b) Temperature-dependent illuminated JV measurements of the nonpolar InGaN MQW solar cell. (c) Extracted V_{oc} , J_{sc} , FF, and efficiency values as functions of temperatures.

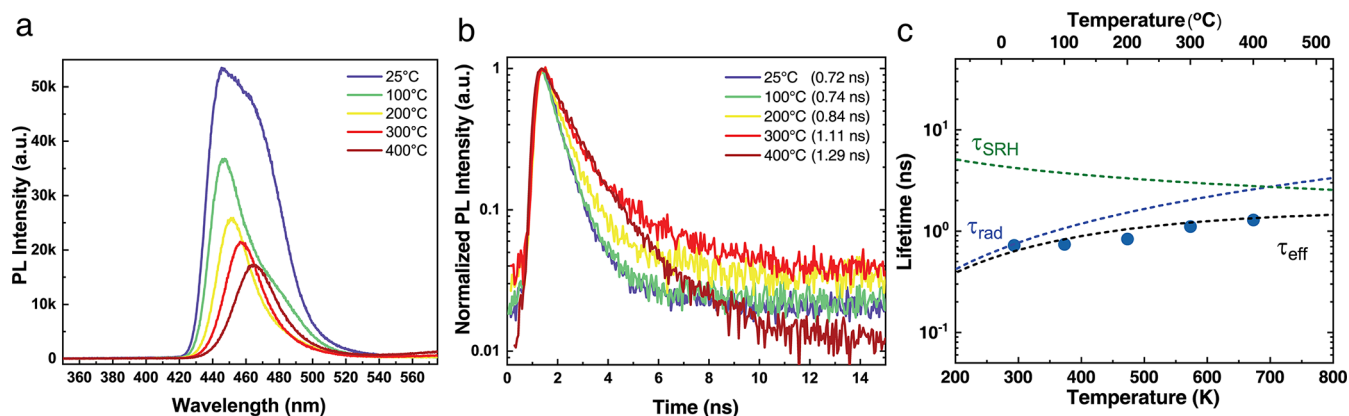


Figure 3. (a) Temperature-dependent photoluminescence (PL) and (b) time-resolved PL measurements of nonpolar InGaN/GaN MQW solar cell devices. (c) Extracted temperature-dependent carrier lifetime for this nonpolar device (blue solid markers). The dashed lines indicate fitting results for τ_{eff} (black), τ_{rad} (blue), and τ_{SRH} (green).

Recently, our group has demonstrated novel polarization-free InGaN QW solar cells with significantly improved carrier collection efficiency using nonpolar m -plane bulk GaN substrates.³³ The new devices offer exciting opportunities for III-nitride solar cells to break the current performance limit particularly at high temperatures.

In this paper, we demonstrate the outstanding high-temperature performance of III-nitride solar cells using polarization-free (i.e., nonpolar) InGaN/GaN multiple quantum wells (MQWs). The InGaN solar cells showed a large working temperature range from RT to 450 °C, with positive temperature coefficients up to 350 °C. The peak value of external quantum efficiencies (EQEs) of the devices showed a 2.5-fold enhancement from RT ($\sim 32\%$) to 450 °C ($\sim 81\%$), which is distinct from all other solar cells ever reported. Time-resolved photoluminescence (TRPL) results reveal that an increase of over 70% in carrier lifetime in nonpolar InGaN MQWs is partly responsible for the enhanced EQE. In addition, a thermal radiation analysis was performed on Si, GaAs, and III-nitride materials, which revealed a unique self-cooling nature of III-nitrides. These results offer new insights and strategies for the design and fabrication of high-efficiency high-temperature PV solar cells using III-nitrides, which will open up not just exciting possibilities but also breakthrough potential for transformative outcomes in solar cell efficiency and deployment.

■ HIGH-TEMPERATURE CHARACTERIZATIONS OF THE NONPOLAR INGAN/GAN MQW SOLAR CELLS

Figure 1(a) presents the schematic crystal planes of the polar c -plane (top) and the nonpolar m -plane GaN (bottom). Figure 1(b) shows the schematic zoom-in energy band diagrams of the active InGaN/GaN MQW regions of the two crystal planes. It can be seen that due to the large polarization-related effects, the energy band diagram of the MQWs on the conventional polar c -plane GaN is tilted. In contrast, the energy band diagram of the MQWs on the polarization-free nonpolar m -plane is flat. The distinct energy band profiles between two cases will have significant impacts on the carrier transport, leading to very different solar cell device performance under high temperatures. This will be discussed in detail in the following section. The complete energy band diagrams are shown in Figure S1. Figure 1(c) shows the schematic device structure for the fabricated nonpolar InGaN solar cell, while Figure 1(d–f) show the cross-section high-angle annular dark-field (HAADF) scanning transmission electron microscopy (STEM) images of the nonpolar m -plane InGaN/GaN MQW solar cell structure with 20 periods of nominal 6 nm InGaN and 10 nm GaN MQWs. The average thickness of one period of InGaN QW and GaN barrier is around 17.5 nm. The hexagonal wurtzite structure of GaN can be clearly identified from Figure 1(e) and (f). Very high quality InGaN/GaN MQW structures were obtained, as evidenced by the STEM images and high-resolution X-ray diffraction (HRXRD) results

in Figure S2. The energy-dispersive X-ray (EDX) element mapping of In (displayed in blue false color) and the corresponding EDX spectrum profile along the growth direction are shown in Figure S3. The details of the epitaxial growth and fabrication processes for the solar cells can be found in the Methods section.

The EQE performance of the fabricated nonpolar InGaN/GaN solar cell was characterized under various temperatures from 25 to 450 °C, and the results are shown in Figure 2(a). As the temperature increases, the peak EQEs of the nonpolar InGaN solar cell continuously increase from ~32% at 25 °C to ~81% at 450 °C. This is distinct from previous reports,^{34,35} as most solar cells show a large degradation in EQE with increasing temperatures. Previous reports on polar InGaN solar cells have also shown that EQE performance degraded as temperature rose.^{28,29} Furthermore, the cutoff wavelengths in the EQE spectral of the nonpolar InGaN solar cells increase dramatically as the temperature increases (i.e., from ~435 nm at 25 °C to ~480 nm at 450 °C), due to the bandgap narrowing at high temperatures. In comparison, the onset wavelengths in the EQE spectra show minimal changes with increasing temperatures. As a result, broadened EQE spectra with enhanced peak EQE values were obtained from the nonpolar InGaN solar cells at high temperatures. This huge enhancement in EQE can also be attributed to three main physical mechanisms: (1) the thermally narrowing bandgap of InGaN along with the enlarged absorbing solar spectrum, leading to significant absorption boost of incident photons; (2) the increased effective carrier lifetime at elevated temperatures. This indicates that longer lifetime enables more carriers to be collected at contacts, which can further facilitate more complete absorption of incident light in the active layers. As shown in Figure 3(c) and Figure S4(c), a higher effective lifetime in the polar *c*-plane device contributed to higher power conversion efficiency and EQE at temperatures below 150 °C in Figure S5. More details on carrier lifetime will be discussed in the following section. The third physical mechanism is (3) the increased diffusion length at elevated temperature, which contributed to the enhanced carrier collection and thus EQE. From the Einstein relation $D = \mu_{\text{MQW}} k_b T / q$, diffusion length can be calculated using $L^2 = D \tau = \mu_{\text{MQW}} k_b T / q \tau$, where μ_{MQW} , k_b , T , q , and τ stand for carrier mobility in MQWs, Boltzmann's constant, temperature, electrical charge, and carrier lifetime, respectively. It is worth noting that μ_{MQW} here is not in bulk material, and thus it is not dominated by phonon scattering.³⁶ Previous work on carrier transport across MQWs demonstrates that effective mobility of both electrons and holes tends to increase through thermal-related carrier processes.³⁷ We can then safely conclude that diffusion length (L) of carriers improves at elevated temperatures by considering the increasing carrier lifetime (τ).

Figure 2(b) shows the temperature-dependent illuminated current density–voltage (J) measurements of the nonpolar InGaN solar cell, while the extracted V_{oc} , J_{sc} fill factor (FF), and power conversion efficiency (eff) as a function of temperatures are plotted in Figure 2(c). The V_{oc} of the nonpolar InGaN solar cell decreases monotonically at a rate of ~2.85 mV/°C in the range of 25–450 °C. This is due to the increased carrier recombination (and thus the increased dark saturation current J_0) as temperature increases, which is consistent with other solar cell reports.^{28,29,38} However, it is noteworthy that the J_{sc} increases monotonically from 0.52 mA/cm² at 25 °C to 1.91 mA/cm² at 450 °C, which suggests a 3.7-

fold enhancement and is closer to the ideal J_{sc} of the Shockley–Queisser limit at the corresponding bandgap (~2.31 mA/cm² at 2.85 eV to ~4.67 mA/cm² at 2.58 eV for an AM1.5G spectrum). This huge increase in J_{sc} also corresponds to the enhanced EQE spectra at elevated temperatures. The FF of the device shows a peak at 200 °C due to the trade-off between V_{oc} and J_{sc} . This rollover phenomena in FF can be ascribed to the trade-off between carrier escape and recombination at high temperatures, which is also reported in other solar cells using double heterostructures.³⁹ As a result, the power conversion efficiency of the nonpolar InGaN solar cell increases monotonically from 0.55% at 25 °C to 0.94% at 350 °C and then falls off to 0.812% at 450 °C. This large enhancement in solar cell efficiency up to 350 °C has never been reported in other solar cell devices. This enhancement of conversion efficiency under elevated temperatures demonstrates the potential and feasibility of III-nitride-based solar cells for high-temperature applications. Based on Shockley–Queisser analysis, the optimal bandgap of the solar cell changes from 1.4 eV at RT to ~2.0 eV at 500 °C.⁴⁰ Although Si and GaAs have nearly optimal bandgaps at RT, they deviate from the optimal values as the temperature rises, resulting in a reduced efficiency. In contrast, with the tunable bandgap property, III-nitrides can be further engineered to match the optimal value of the bandgap for the corresponding temperature (above 450 °C), indicating the huge potential and feasibility of wide-bandgap III-nitrides for high-temperature PV applications.

■ POLARIZATION EFFECTS IN QW CARRIER ESCAPE AT HIGH TEMPERATURES

To explore the fundamental understanding on the high-temperature performance of nonpolar InGaN solar cells, we studied the temperature-dependent optical properties and carrier dynamics for nonpolar and polar InGaN MQW samples using photoluminescence (PL) and TRPL measurements. The power of the pulsed excitation source was chosen to approximate the actual light intensity of solar cells under operation. PL and TRPL spectra from RT to 400 °C of the *m*-plane device are plotted in Figure 3(a) and (b), respectively. Those of the *c*-plane sample are plotted in Figure S4. In Figure 3(a), it is worth noting that strong PL peak intensity was observed for the *m*-plane device even at high temperatures compared to its *c*-plane counterpart. This can be attributed to the strong radiative capability in *m*-plane III-nitride QWs. On the other hand, due to the strong yellow emission from III-nitrides, the PL peaks of MQWs of the *c*-plane sample show interference and are difficult to discern from 300 °C. Therefore, TRPL spectra of the *c*-plane sample at 300 °C have a very low signal/noise ratio and thus can be considered inaccurate to extract carrier lifetime.

The extracted temperature-dependent carrier lifetimes for nonpolar InGaN/GaN MQW devices are plotted in Figure 3(c). The same measurements were also performed on the polar *c*-plane device, and the results are shown in Figure S4(a)–(c) for comparison. It is worthy to note that the lifetime of the *m*-plane device rises as the temperature increases and increases by over 70% at 400 °C compared to that at RT. We attributed this surprising phenomenon to the strong radiative recombination ability of *m*-plane InGaN MQWs. This also corresponds to the relatively strong PL emission at elevated temperatures for the *m*-plane device shown in Figure 3(a). It has been observed and confirmed by

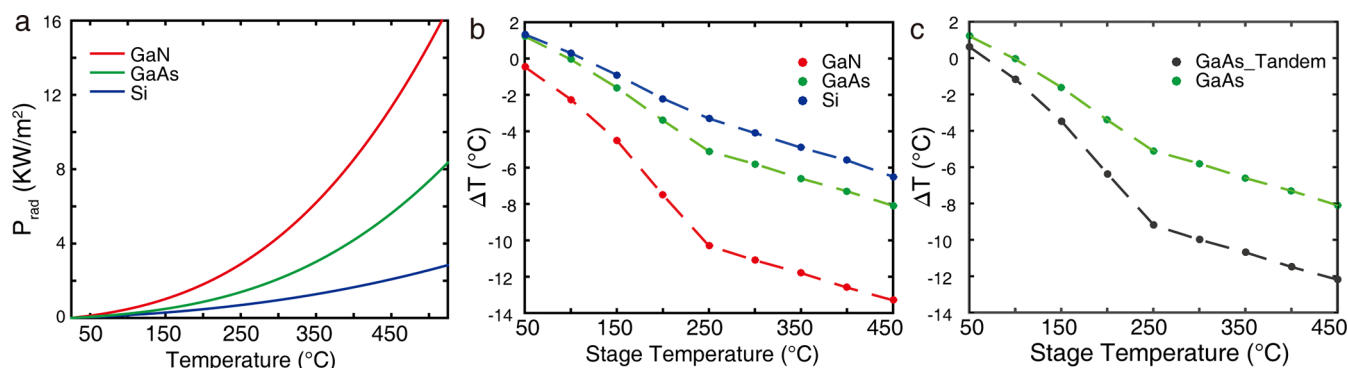


Figure 4. (a) Net thermal radiation power density P_{rad} for GaN, GaAs, and Si calculated from experimentally measured thermal emissivity. (b) Calculated temperature difference between the InGaN solar cell sample and the heating stage temperatures at different heating stage temperatures. The temperature differences of GaAs and Si are also plotted for reference. (c) Calculated temperature difference between GaN–GaAs tandem cell sample and heating stage temperature at different heating stage temperatures. The temperature difference of GaAs is also plotted for reference. It clearly shows that with III-nitride as the top cell, the operating temperature of the underlying GaAs cell reduces effectively.

previous literature that *m*-plane InGaN QWs have a large radiative recombination rate compared to *c*-plane counterparts.^{41–43} On the other hand, the *c*-plane device has shown an opposite trend compared to the nonpolar device.

The temperature-dependent carrier lifetimes for nonpolar and polar InGaN/GaN MQW devices are also fitted to a carrier recombination model to determine the main recombination mechanism(s) at different temperatures. Three major carrier mechanisms are considered in this analysis: radiative recombination (lifetime τ_{rad}), Shockley–Read–Hall recombination (lifetime τ_{SRH}), and thermionic emission (lifetime τ_{th}). For the QW structure we used in the experiment (6 nm InGaN QW and 10 nm GaN barrier layer), the thermionic escape was found to be the dominant carrier transport mechanism,⁴⁴ where the tunneling escape of carriers was treated as a minor concern. The analytical expressions of different temperature-dependent τ_{rad} , τ_{SRH} , and τ_{th} are described in previous literature.⁴⁵ For simplicity, the aforementioned temperature-dependent lifetimes can be expressed as

$$\tau_{\text{rad}} \propto C_{\text{rad}} T^{1.5} \quad (1)$$

$$\tau_{\text{SRH}} \propto C_{\text{SRH}} T^{-0.5} \quad (2)$$

$$\tau_{\text{th}} \propto C_{\text{th}} T^{-0.5} e^{\Delta E/kT} \quad (3)$$

where ΔE is the barrier height for carriers and C_{rad} , C_{SRH} , and C_{th} are temperature-independent coefficients for radiative recombination, Shockley–Read–Hall recombination, and thermionic emission processes.^{43,45} Then the effective lifetime τ_{eff} contains all three recombination processes:

$$\frac{1}{\tau_{\text{eff}}} = \frac{1}{\tau_{\text{rad}}} + \frac{1}{\tau_{\text{SRH}}} + \frac{1}{\tau_{\text{th}}} \quad (4)$$

Solid markers in Figure 3(c) and Figure S4(c) represent the effective lifetime obtained from TRPL measurements, while dashed lines indicate the fitting curves to eqs 1–4. It is worth noting that τ_{rad} is the only recombination process that positively correlates with temperature.^{45,46} For the *m*-plane device, τ_{eff} increases from 0.72 ns at 25 $^{\circ}\text{C}$ to 1.29 ns at 400 $^{\circ}\text{C}$, which is over 70% larger. TRPL results suggest that the *m*-plane device is mostly dominated by radiative recombination at all measured temperature ranges. In addition, this excitonic nature of the radiative recombination in the *m*-plane sample can be directly attributed to the polarization-free quantum well

structure. The larger overlap of wave functions and higher exciton binding energy due to the nonpolar QWs have been reported to contribute to the enhanced radiative ability.⁴³ The radiative recombination lifetime will then increase due to this temperature-dependent excitonic nature of radiative recombination. In addition, the thermionic emission process is not applicable in analyzing effective lifetime in nonpolar devices, and SRH recombination also plays a role at high temperatures since extracted PL lifetimes of the *m*-plane device are not completely proportional to $T^{1.5}$. This prolonged carrier lifetime also accounts for the enhanced J_{sc} at high temperatures.

On the other hand, the *c*-plane device has shown the opposite trend compared to the nonpolar device. This indicates that SRH recombination and thermionic emission processes play a critical role at high temperatures. In addition, the radiative recombination lifetime of the *c*-plane device is also about 1 order of magnitude larger than that of the *m*-plane device. This also corresponds to the strong polarization effect in *c*-plane QWs, leading to lower radiative probability.

■ SELF-COOLING EFFECTS IN GAN USING THERMAL RADIATION ANALYSIS

To further investigate the physical nature of high-temperature performance of III-nitrides, the emissivity measurement was taken and a thermal radiation power analysis was carried out where Si and GaAs were used as references, as shown in Figure S6. The calculations are performed by a finite-difference-based thermal simulator, taking into account the solar cell absorbed power under AM 1.5G illumination, the heat dissipation by thermal radiation of the cell, and the nonradiative heat dissipation to the environment by conduction and convection. The details on the calculation can be found in ref 47. Figure 4a shows the calculated temperature difference between the InGaN solar cell and the heating stage at various heating stage temperatures. As a comparison, the temperature differences for GaAs and Si are also plotted. As shown in Figure 4b, the temperature difference (absolute value) for III-nitride is significantly larger than the others and increases as the stage temperature increases. This is mainly due to the increased heat dissipation through thermal radiation of the GaN cell at elevated temperatures presented in Figure 4a. Similar trends are also observed for GaAs and Si cells. However, the temperature differences of these two cells are much smaller

than the GaN cell, due to the weaker heat dissipation through thermal radiation.

This outstanding heat dissipation capability through thermal radiation of III-nitride can also contribute to the low temperature coefficient of V_{oc} of the InGaN-based solar cell compared to Si and GaAs. From the one-diode model, the expression for V_{oc} is $V_{oc} = \frac{nkT}{q} \ln\left(\frac{J_{sc}}{J_0} + 1\right)$, where n is the ideality factor, q is the electron charge, and J_0 is the dark saturation current density. Then the temperature coefficient of V_{oc} is defined as

$$C_{V_{oc}} \equiv \frac{1}{V_{oc}^{300K}} \frac{\partial V_{oc}}{\partial T} = \frac{1}{T} + \frac{1}{V_{oc}^{300K}} \frac{nkT}{q} \left(\frac{1}{J_{sc}} \frac{\partial J_{sc}}{\partial T} - \frac{1}{J_0} \frac{\partial J_0}{\partial T} \right) \quad (5)$$

The comparisons between (a) measured and ideal V_{oc} , (b) measured and calculated dV_{oc}/dT , and (c) measured and calculated $C(V_{oc})$ are shown in Figure S7. It is worth noting that J_0 is extremely sensitive to the temperature,⁴⁸ as defined as $J_0 = CT^3 \exp\left(-\frac{E_g}{kT}\right)$, where C is the material parameter and E_g is the bandgap energy. Therefore, under the same stage/ambient temperature, the higher temperature difference (in absolute value) suggests less dark current density J_0 and less thermal bandgap narrowing. Thus, for III-nitrides, the decrease in V_{oc} will be suppressed and $C_{V_{oc}}$ is smaller. For the nonpolar InGaN solar cell, it is $-0.136\%/K$ for V_{oc} and is also consistent with previous reports^{29,35} and far better than those of GaAs ($-0.238\%/K$) and Si cells ($-0.329\%/K$).^{29,49} The lower thermal radiation power density of Si compared to GaAs also corresponds to the lower temperature coefficient of V_{oc} (higher in absolute value). Consequently, this self-cooling effect of III-nitrides can also potentially be beneficial for InGaN/III-V tandem or multijunction cells. The employment of an InGaN top cell is capable of reducing the operating temperature of the underlying III-V cells at elevated temperatures, as evidenced in Figure 4(c).

CONCLUSIONS

In conclusion, we demonstrated a high-performance nonpolar InGaN MQW solar cell with great potential for high-temperature PV applications (e.g., >350 °C). The single-junction nonpolar m -plane InGaN solar cell exhibited a large positive temperature coefficient for EQE and PV efficiency from RT to 350 °C, which is distinct from any solar cells ever reported. A 70% efficiency enhancement was observed from RT to 350 °C in this nonpolar InGaN cell. This superior thermal performance is also attributed to several factors: (i) improved material quality through the homoepitaxial growth enabled by single-crystal substrates; (ii) enhanced radiative capability due to nonpolar crystal orientation, thus improved effective lifetime of the photogenerated carriers in the QWs; and (iii) narrowed large energy bandgap at high temperatures, offering better matching with the solar spectrum. Furthermore, thermal radiation heat dissipation analysis revealed a unique self-cooling effect of III-nitrides. Near-unity emissivity of GaN resulted in a significant reduction of the device temperature, which leads to the reduced V_{oc} loss in InGaN solar cells. The self-cooling III-nitride top cell could serve as a heat shield for the underlying subcell(s) by reducing their device temperatures in the tandem design. These results offer new insights and strategies for the design and fabrication of high-efficiency

high-temperature PV solar cells using III-nitrides, which will open up exciting new applications such as in space applications and potentially lead to transformative outcomes in solar cell efficiency and deployment.

METHODS

Growth and Structure Parameters of Nonpolar InGaN Solar Cells. InGaN MQW solar cells on nonpolar m -plane substrates were grown by conventional metal-organic chemical vapor deposition. The growth condition was designed to achieve an indium incorporation around 15% in samples. The designed device consists of 1 μm Si-doped n-GaN ($[\text{Si}] = 5 \times 10^{18} \text{ cm}^{-3}$), 10 nm highly Si-doped n^+ -GaN ($[\text{Si}] = 1 \times 10^{19} \text{ cm}^{-3}$), 20 periods of InGaN (6 nm)/GaN (10 nm) MQWs, 30 nm Mg-doped smooth p^+ -GaN ($[\text{Mg}] = 1 \times 10^{19} \text{ cm}^{-3}$), 120 nm Mg-doped p-GaN ($[\text{Mg}] = 3 \times 10^{19} \text{ cm}^{-3}$), and a 10 nm highly Mg-doped p^+ -GaN contact layer ($[\text{Mg}] = 1 \times 10^{20} \text{ cm}^{-3}$). None of these devices is coated with traditional indium tin oxide or current spreading layers.

Solar Cell Fabrication and Characterization. InGaN solar cell samples were processed into 1 mm \times 1 mm mesas by standard contact lithography and inductively coupled plasma etching. Ti/Al/Ni/Au and Ni/Au grid contacts deposited via electron beam evaporation were employed as n and p metal contacts, respectively. More structural and fabrication details on InGaN solar cells can be found in refs 15 and 33.

HRXRD Measurement. The nonpolar InGaN solar cell sample was characterized by high-resolution X-ray diffraction measurement using a PANalytical X'Pert Pro Materials Research X-ray diffractometer (MRD) system with Cu $K\alpha$ radiation. A hybrid monochromator and triple-axis module were used for the incident and diffracted beam optics, respectively.

FIB and STEM Imaging. The nonpolar InGaN solar cell specimens for STEM imaging were prepared with an FEI Nova 200 dual-beam FIB system with a Ga ion source. A JEOL-ARM200F scanning transmission electron microscope operated at 200 kV and equipped with double aberration correctors for both probe-forming and imaging lenses was used to perform HAADF imaging. The compositional distribution of In element in MQW layers was accomplished by acquiring the EDX spectroscopic spectra of In element.

Illuminated Current Density–Voltage and EQE Measurement. Solar cell parameters such as the open-circuit voltage, fill factor, and power conversion efficiency were extracted from LIV measurements taken using an Oriel Class A solar simulator. The Newport Class A solar simulator generates a 4-in.-diameter collimated beam using a xenon arc lamp and a series of filters designed to provide 0.1 W cm^{-2} at the surface of the testing stage. All JV curves of InGaN and GaAs cells were taken at a 1 sun condition AM1.5G spectrum.

EQE measurement data were collected under short-circuit conditions using an Oriel QEPVSI quantum efficiency measurement system and calibrated with a reference Si photodetector. This system is composed of a 150 W xenon arc lamp coupled with a Cornerstone 260 1/4m monochromator.

A Linkam HFS600-PB4 stage capable of heating the samples up to 600 °C was used to perform the temperature-dependent measurements. For both the EQE and current–voltage (I – V) measurements, the temperature of the stage was increased from room temperature to 450 °C in steps of 25–50 °C with a ramp rate of 10–20 °C/min. Once the desired temperature

was reached, the sample was kept at the specified temperature for another 3 min. The experimental setup did not allow for the simultaneous acquisition of the temperature-dependent EQE and I - V .

Photoluminescence and Time-Resolved Photoluminescence Measurements. PL and TRPL measurements were done using a home-built system, where a picosecond 405 nm pulsed laser diode (PDL 800-B) was used as excitation source. A very low excitation power density was used in order to extract carrier dynamics for the device operating as a solar cell. PL spectra were collected by a Si array detector coupled with a Horiba monochromator (TRIAx 320). TRPL was measured by a time-correlated single-photon counting system (TCSPC). A Si photomultiplier tube detector is attached at the other output port of the monochromator, and its signal is then recorded by the TCSPC board (SPC130 module).

Transmission and Reflection Spectra Measurement. The transmission and reflectance spectra of the fabricated nonpolar InGa_N solar cell sample were characterized with a LAMBDA 950/1050 UV/vis/NIR spectrophotometer from PerkinElmer.

Emissivity Measurement. The thermal radiation power density was obtained from experimentally characterized thermal emissivity of the solar cells by using a Fourier transform infrared spectrometer (Thermo Scientific Nicolet 6700). The absorptivity/emissivity spectra were obtained by subtracting the reflectance and transmittance from unity. The Ga_N, GaAs, and Si substrates were all around 300 μm , while the thickness of Ga_N grown on the sapphire was around 3 μm .

Simulation of Band Diagrams. The energy band diagrams of InGa_N/Ga_N double heterostructures were simulated using Silvaco ATLAS software. They all contain a 6 nm absorbing layer and a 10 nm barrier. The band structure parameters, the conduction, and valence band offsets of InGa_N/Ga_N DHs were obtained from Huang et al.,³³ respectively. Silvaco ATLAS is a commercial device simulation tool based on the drift-diffusion model. MQW simulation is based on a parabolic quantum well model implemented within Silvaco ATLAS. The bound state energies are calculated solving the Schrödinger equation along discrete slices in the quantization direction.

■ ASSOCIATED CONTENT

📄 Supporting Information

The Supporting Information is available free of charge on the ACS Publications website at DOI: 10.1021/acsp Photonics.9b00655.

Schematic energy band diagram, HRXRD ω - 2θ scan curve, HAADF-STEM image and corresponding EDX mapping, temperature-dependent PL and TRPL, temperature-dependent EQE and illuminated JV measurements, and thermal emissivity measurements (PDF)

■ AUTHOR INFORMATION

Corresponding Authors

*E-mail: shanhui@stanford.edu.

*E-mail: yuji.zhao@asu.edu.

ORCID

Xuanqi Huang: 0000-0002-7085-4162

Wei Li: 0000-0002-2227-9431

Houqiang Fu: 0000-0002-1125-8328

Hong Chen: 0000-0003-4963-7515

Author Contributions

‡X.H. and W.L. contributed equally to this work.

Notes

The authors declare no competing financial interest.

■ ACKNOWLEDGMENTS

This work was supported by an Early Career Faculty grant from NASA's Space Technology Research Grants Program (Grant No. ECF NNX15AU48G). W.L. and S.F. acknowledge the support of the Department of Energy (Grant No. DE-FG02-07ER46426). S.P.D. and S.N. acknowledge the support of the Solid State Lighting and Energy Electronics Center (SSLEEC) at University of California Santa Barbara (UCSB). The authors would like to thank Prof. Yong-Hang Zhang and Prof. Christiana Honsberg for their constructive comments and suggestions. We gratefully acknowledge the use of facilities within the LeRoy Eyring Center for Solid State Science and the ASU Nanofab at Arizona State University. This work was supported, in part, by NSF award number NNCI-1542160.

■ REFERENCES

- (1) Ercol, C. J.; Jenkins, J.; Dakermanji, G.; Santo, A. G.; Mason, L. S. In *Collection of Technical Papers. 35th Intersociety Energy Conversion Engineering Conference and Exhibit (IECEC) (Cat. No.00CH37022)*; 2000; Vol. 1, pp 449–459.
- (2) Sulima, O. V.; Sims, P. E.; Cox, J. A.; Mauk, M. G.; Mueller, R. L.; Reedy, R. C.; Khammadv, A. M.; Paulson, P. D.; Landis, G. A. In *Proceedings of 3rd World Conference on Photovoltaic Energy Conversion*, 2003; 2003; Vol. 1, pp 737–740.
- (3) Landis, G. A. In *2008 33rd IEEE Photovoltaic Specialists Conference*; 2008; pp 1–5.
- (4) Merritt, D.; Houlihan, S.; Raffaele, R. P.; Landis, G. A. In *Conference Record of the Thirty-first IEEE Photovoltaic Specialists Conference*, 2005; 2005; pp 552–555.
- (5) Branz, H.; Regan, W.; Gerst, K.; Borak, J.; Santori, E. *Energy Environ. Sci.* **2015**, *8*, 3083–3091.
- (6) Goodnick, S. M.; Ponce, F.; Doolittle, W. A.; Honsberg, C.; Vasileska, D.; Choudhry, S.; Arena, C.; Gleckman, P. In *Optics for Solar Energy, OSE 2014*; Optical Society of America (OSA), 2014.
- (7) Tyagi, V. V.; Kaushik, S. C.; Tyagi, S. K. *Renewable Sustainable Energy Rev.* **2012**, *16*, 1383–1398.
- (8) Maros, A.; Gangam, S.; Fang, Y.; Smith, J.; Vasileska, D.; Goodnick, S.; Bertoni, M. I.; Honsberg, C. B. In *Photovoltaic Specialist Conference (PVSC), 2015 IEEE 42nd*; 2015; pp 1–5.
- (9) Landis, G. A. In *13th Space Photovoltaic Research and Technology Conference (SPRAT 13)*; 1994.
- (10) Bittner, Z. S.; Forbes, D. V.; Nesnidal, M.; Hubbard, S. M. In *2011 37th IEEE Photovoltaic Specialists Conference*; 2011; pp 001959–001964.
- (11) Perl, E. E.; Simon, J.; Geisz, J. F.; Lee, M. L.; Friedman, D. J.; Steiner, M. A. *IEEE J. Photovolt.* **2016**, *6*, 1345–1352.
- (12) Steiner, M. A.; Geisz, J. F.; Friedman, D. J.; Olavarria, W. J.; Duda, A.; Moriarty, T. E. In *2011 37th IEEE Photovoltaic Specialists Conference*; 2011; pp 002527–002532.
- (13) Neudeck, P. G.; Okojie, R. S.; Chen, L.-Y. *Proc. IEEE* **2002**, *90*, 1065–1076.
- (14) Marlow, G. S.; Das, M. B.; Tongson, L. *Solid-State Electron.* **1983**, *26*, 259–266.
- (15) Huang, X.; Fu, H.; Chen, H.; Lu, Z.; Baranowski, I.; Montes, J.; Yang, T.-H.; Gunning, B. P.; Koleske, D.; Zhao, Y. *Appl. Phys. Lett.* **2017**, *111*, 233511.
- (16) Wu, J. *J. Appl. Phys.* **2009**, *106*, No. 011101.
- (17) Wu, J.; Walukiewicz, W.; Yu, K. M.; Shan, W.; Iii, J. W. A.; Haller, E. E.; Lu, H.; Schaff, W. J.; Metzger, W. K.; Kurtz, S. *J. Appl. Phys.* **2003**, *94*, 6477–6482.
- (18) Huang, X.; Fu, H.; Chen, H.; Lu, Z.; Ding, D.; Zhao, Y. *J. Appl. Phys.* **2016**, *119*, 213101.

- (19) Muth, J. F.; Lee, J. H.; Shmagin, I. K.; Kolbas, R. M.; Casey, H. C.; Keller, B. P.; Mishra, U. K.; DenBaars, S. P. *Appl. Phys. Lett.* **1997**, *71*, 2572–2574.
- (20) Bhuiyan, A. G.; Sugita, K.; Hashimoto, A.; Yamamoto, A. *IEEE J. Photovolt.* **2012**, *2*, 276–293.
- (21) Jani, O.; Ferguson, I.; Honsberg, C.; Kurtz, S. *Appl. Phys. Lett.* **2007**, *91*, 132117.
- (22) Dahal, R.; Pantha, B.; Li, J.; Lin, J. Y.; Jiang, H. X. *Appl. Phys. Lett.* **2009**, *94*, No. 063505.
- (23) Farrell, R. M.; Neufeld, C. J.; Cruz, S. C.; Lang, J. R.; Iza, M.; Keller, S.; Nakamura, S.; DenBaars, S. P.; Mishra, U. K.; Speck, J. S. *Appl. Phys. Lett.* **2011**, *98*, 201107.
- (24) Arif, M.; Elhuni, W.; Streque, J.; Sundaram, S.; Belahsene, S.; El Gmili, Y.; Jordan, M.; Li, X.; Patriarche, G.; Slaoui, A.; Migan, A.; Abderrahim, R.; Djebbour, Z.; Voss, P. L.; Salvestrini, J. P.; Ougazzaden, A. *Sol. Energy Mater. Sol. Cells* **2017**, *159*, 405–411.
- (25) Dahal, R.; Li, J.; Aryal, K.; Lin, J. Y.; Jiang, H. X. *Appl. Phys. Lett.* **2010**, *97*, No. 073115.
- (26) Kuwahara, Y.; Fujii, T.; Sugiyama, T.; Iida, D.; Isobe, Y.; Fujiyama, Y.; Morita, Y.; Iwaya, M.; Takeuchi, T.; Kamiyama, S.; Akasaki, I.; Amano, H. *Appl. Phys. Express* **2011**, *4*, No. 021001.
- (27) Zhao, L.; Detchprohm, T.; Wetzels, C. *Appl. Phys. Lett.* **2014**, *105*, 243903.
- (28) Williams, J. J.; McFavilen, H.; Fischer, A. M.; Ding, D.; Young, S.; Vadiiee, E.; Ponce, F. A.; Arena, C.; Honsberg, C. B.; Goodnick, S. M. *IEEE J. Photovolt.* **2017**, *7*, 1646–1652.
- (29) Lien, D.-H.; Hsiao, Y.-H.; Yang, S.-G.; Tsai, M.-L.; Wei, T.-C.; Lee, S.-C.; He, J.-H. *Nano Energy* **2015**, *11*, 104–109.
- (30) Huang, X.; Chen, H.; Fu, H.; Baranowski, I.; Montes, J.; Yang, T.-H.; Fu, K.; Gunning, B. P.; Koleske, D. D.; Zhao, Y. *Appl. Phys. Lett.* **2018**, *113*, No. 043501.
- (31) Wierer, J. J.; Fischer, A. J.; Koleske, D. D. *Appl. Phys. Lett.* **2010**, *96*, No. 051107.
- (32) Neufeld, C. J.; Cruz, S. C.; Farrell, R. M.; Iza, M.; Lang, J. R.; Keller, S.; Nakamura, S.; DenBaars, S. P.; Speck, J. S.; Mishra, U. K. *Appl. Phys. Lett.* **2011**, *98*, 243507.
- (33) Huang, X.; Fu, H.; Chen, H.; Zhang, X.; Lu, Z.; Montes, J.; Iza, M.; DenBaars, S. P.; Nakamura, S.; Zhao, Y. *Appl. Phys. Lett.* **2017**, *110*, 161105.
- (34) Williams, J. J.; McFavilen, H.; Fischer, A. M.; Ding, D.; Young, S. R.; Vadiiee, E.; Ponce, F. A.; Arena, C.; Honsberg, C. B.; Goodnick, S. M. In *2016 IEEE 43rd Photovoltaic Specialists Conference (PVSC)*; 2016; pp 0193–0195.
- (35) Neufeld, C. J.; Cruz, S. C.; Farrell, R. M.; Iza, M.; Keller, S.; Nakamura, S.; DenBaars, S. P.; Speck, J. S.; Mishra, U. K. *Appl. Phys. Lett.* **2011**, *99*, No. 071104.
- (36) Browne, D. A.; Mazumder, B.; Wu, Y.-R.; Speck, J. S. *J. Appl. Phys.* **2015**, *117*, 185703.
- (37) Toprasertpong, K.; Goodnick, S. M.; Nakano, Y.; Sugiyama, M. *Phys. Rev. B: Condens. Matter Mater. Phys.* **2017**, *96*, DOI: 10.1103/PhysRevB.96.075441.
- (38) Perl, E. E.; Simon, J.; Geisz, J. F.; Olavarria, W.; Young, M.; Duda, A.; Friedman, D. J.; Steiner, M. A. *IEEE J. Photovolt.* **2016**, *6*, 770–776.
- (39) Becker, J. J.; Campbell, C. M.; Tsai, C. Y.; Zhao, Y.; Lassise, M.; Zhao, X. H.; Boccard, M.; Holman, Z. C.; Zhang, Y. H. *IEEE J. Photovolt.* **2018**, *8*, 1–6.
- (40) Wilcox, J. R. Solar cell temperature dependent efficiency and very high temperature efficiency limits. Ph.D. thesis, Purdue University, Indiana, USA, 2013.
- (41) Marcinkevicius, S.; Kelchner, K. M.; Kuritzky, L. Y.; Nakamura, S.; DenBaars, S. P.; Speck, J. S. *Appl. Phys. Lett.* **2013**, *103*, 111107.
- (42) Badcock, T. J.; Ali, M.; Zhu, T.; Pristovsek, M.; Oliver, R. A.; Shields, A. J. *Appl. Phys. Lett.* **2016**, *109*, 151110.
- (43) Langer, T.; Klisch, M.; Ketzner, F. A.; Jönen, H.; Bremers, H.; Rossow, U.; Meisch, T.; Scholz, F.; Hangleiter, A. *Phys. Status Solidi B* **2016**, *253*, 133–139.
- (44) Lang, J. R.; Young, N. G.; Farrell, R. M.; Wu, Y.-R.; Speck, J. S. *Appl. Phys. Lett.* **2012**, *101*, 181105.
- (45) Zhao, X. H.; Liu, S.; Campbell, C. M.; Zhao, Y.; Lassise, M. B.; Zhang, Y. H. *IEEE J. Photovolt.* **2017**, *7*, 913–918.
- (46) Perl, E. E.; Kuciauskas, D.; Simon, J.; Friedman, D. J.; Steiner, M. A. *J. Appl. Phys.* **2017**, *122*, 233102.
- (47) Li, W.; Shi, Y.; Chen, K.; Zhu, L.; Fan, S. *ACS Photonics* **2017**, *4*, 774–782.
- (48) Nell, M. E.; Barnett, A. M. *IEEE Trans. Electron Devices* **1987**, *34*, 257–266.
- (49) Singh, P.; Ravindra, N. M. *Sol. Energy Mater. Sol. Cells* **2012**, *101*, 36–45.